Multiphysics approach for fluid and charge transport in paper-based microfluidics

Nicolás Franck · **Claudio L. A. Berli** · **Pablo A. Kler** · **Raúl Urteaga**

Abstract A multiphysic model that simultaneously describe different transport phenomena in porous media is presented. The porous matrix is regarded as a bundle of periodically constricted tubes, whose pore radius distribution is described by a probability density function (PDF). The mathematical basis and the experimental validation of the model are reported. Two different materials frequently used in paper-based microfluidics were used: Whatman #1 and Muntktell 00A filter papers. These substrates were studied by capillary imbibition, hydrostatic pressure-driven flow, and electrical resistance measurements. Different PDFs were evaluated to represent the output of these experiments, and their predictions were quantified by using a Chi-Square test. The model was able to simultaneously describe the three transport phenomena by using the log-normal PDF with two statistical parameters: mean and variance. The formulation avoids including the tortuosity of the flow path, which is commonly employed as an adjusting parameter. The multiphysics model was also successfully used to calculate the parameters of single-physics models, such as Darcy's permeability and Lucas-Washburn diffusion coefficient. Furthermore, after obtaining a suitable PDF, the proposed model can be applied to different porous materials, as well as to the design of complex paper-based microfluidic devices that combine several types of papers.

Keywords Paper-based microfluidics · Capillary flow · Fluid transport model · Pore radius distribution

1 Introduction

Understanding the microstructure and physicochemical properties of porous media is of great importance for several fields in order to carry out rational design and optimization processes (Schaumburg et al., 2018a; Masoodi and Pillai, 2010; Gerlero et al., 2022). Particularly, microfluidic paper-based analytical devices (μPADs) have gained remarkable popularity with their applications in chemistry, medicine, genetics, and cell biology, among others (Modha et al., 2021; Tesfaye and Hussen, 2022). However, currently there exists the need to accelerate the introduction of μPADs into the market and public health systems. Reliable and useful mathematical models are required to predict the behavior of μPAD under different operative situations, which involve phenomena such as capillary imbibition, pressure-driven flow (Shen et al., 2021), electroosmotic flow, and electric current (Mai et al., 2019; Franck et al., 2021), plus those related to the transport and reaction of different chemical species. Porous media in general, and particularly paper substrates, have being systematically studied for fluid transport and, over the last century, several mathematical models have been proposed together with attempts for experimental validation. The aim was to define and characterize parameters that can act as intrinsic descriptors of pore structure and their influence on the macroscopic behavior of porous media for fluidic and electric phenomena (MacDonald, 2018). In the pioneer works of Lucas (1918) and Washburn (1921), paper was modelled as a single circular and

Nicolás Franck · Pablo A. Kler
Centro de Investigación en Métodos Computacionales (CIMEC, UNL–CONICET).
Predio CCT CONICET Santa Fe. RN 168, Santa Fe 3000, Argentina

Claudio.L.A Berli
Instituto de Desarrollo Tecnológico para la Industria Química (INTEC, UNL – CONICET).
Predio CCT CONICET Santa Fe. RN 168, Santa Fe 3000, Argentina

Pablo A. Kler
Departamento de Ingeniería en Sistemas de Información, FRSF-UTN, Santa Fe, Argentina.

Raúl Urteaga
Instituto de Física del Litoral (IFIS Litoral, UNL–CONICET).
Guemes 3450, S3000GLN Santa Fe, Argentina.
E-mail: urteagar@santafe-conicet.gov.ar

uniform cross section capillary tube. Later on, Kozeny (1927) modelled the porous medium as a bundle of capillary tubes of equal length, with not necessarily circular cross-section, neglecting the fluid velocity normal to the tube's axis. More recently, Bear (1972) represented the flow through a parallelepiped body of porous medium in a laminar flow regime, with circular capillary tubes of fixed diameter, by using the Hagen-Poiseuille law, and Scheidegger (1974) related the distribution of diameters of the capillary tubes to the pore size distribution. During the last years, models composed of a network of interconnected capillary channels were proposed (Gruener et al., 2012; Cummins et al., 2017).

Regarding capillary-driven flow, numerous experimental works have been documented as input for more complex interpretations of Lucas-Washburn dynamics. For example, Böhm et al. (2014) studied the influence of the fiber material and porosity on the efficiency of capillary-driven flow of aqueous solutions. Elizalde et al. (2016) made systematic wetting cycles and observed the trends in the imbibition dynamics due to changes in the inner structure of Whatman # 1 paper. More recently, Lei et al. (2021) presented a model for the dynamics of capillary flow in periodically (sinusoidal) undulated channels, predicting the capillary rising dynamics. Additionally, the speed of meniscus advance as a function of capillary radius (variable) was described by Gorce et al. (2016). A similar process was documented for electrical properties, as it is described in the first works of Archie (1942), where the author proposed an empirical relationship that links the experimentally measured factors to the electrical conductivity of both the saturated rocks and the solution inside the void space. There were also different proposed relationships between the electrical conductivity of saturated porous media and pore fluid conductivity, like those based on effective medium (Bussian, 1983), percolation (Ghanbarian et al., 2014) and cylindrical tubes (Herrick and Kennedy, 1994).

As it was mentioned above, an important number of mathematical models and the associated experiments have been presented in the literature, aiming to reproduce only a particular phenomenon, such as Darcy flow (Mora et al., 2019), capillary imbibition (Piovesan et al., 2022; Elizalde et al., 2016; Salama et al., 2021), electrical resistance (Mai et al., 2019), electroomotic flow and electrophoretic migration (Schaumburg et al., 2020), or advective non-reactive transport (Schaumburg et al., 2018b; Urteaga et al., 2018). With the aforementioned exceptions, most of these models consider the paper porous structure as a bundle of non-interconnected capillary tubes and, on a general basis, the idea requires three different parameters: (i) porosity (ϕ), which is a direct physical parameter representing the fractions of void volume over the total volume of the substrate; (ii) Darcy permeability (K), which represents the constant of proportionality between the pressure gradient and the fluid flow under Darcy flow conditions; and (iii) tortuosity (τ), which is defined as the ratio of the hypothetical average length of the capillary tubes to the length of the substrate in the flow direction (Duda et al., 2011). These three parameters clearly differ on their nature and accessibility. While ϕ and K can be measured via several techniques (Berg, 2014; Bear and Cheng, 2010), τ is a mathematical abstraction attached to the hypotheses of the model of non-interconnected capillary tubes (Liu et al., 2018; Cai et al., 2014; Duda et al., 2011).

It has been shown experimentally that capillary-driven infiltration in paper strips follows the simple Lucas-Washburn dynamics, $L^2 = Dt$, where L is the position of the imbibition front at time t and is D a dynamic coefficient that depends on the characteristics of both the fluid and porous matrix. Actually, D is related to the Darcy permeability by $D = K\Delta P/\mu$, where ΔP is the driving pressure difference, and μ is the fluid viscosity. Further descriptions of D in terms of the paper microstructure require models for both K and ΔP.

The simplest physical representation of the porous space is the capillary bundle model: straight, parallel, and not interconnected pores of hydrodynamic radius r_h, for which the permeability is $K = r_h^2/8$. Concerning the pressure, the Laplace equation is adopted, $\Delta P = 2\gamma cos\theta/r_c$, where γ is the surface tension, and θ is the meniscus contact angle, and r_c is the capillary radius. Besides, it is customarily assumed that $r_h = r_c = r_{pore}$, where r_{pore} is expected to be the actual pore radius of the porous matrix. Then, the dynamic coefficient results $D = r_{pore}\gamma cos\theta/(4\mu)$. The practical problem that emerges is that water infiltration in paper (namely Whatman #1, nominal pore radius about $11\mu m$) is much slower than the value predicted by the above expression. Conversely, the effective pore radius (r_{eff}) that satisfies the experimental value of D is abnormally small (about $100nm$).

A straightforward correction is the incorporation of the tortuosity τ, aimed to account for the non-linear fluid paths of the cellulose matrix. Thus, considering $r_{eff} = r_{pore}/\tau^2$, the tortuosity of Whatman #1 ($r_{pore} \sim 11\mu m$) results $\tau \sim 10$, which is much larger than the expected for the configuration of cellulose fibers in paper. A second drawback of this approach is that the tortuosity values required to fit experimental data, strongly depends on the type of experiments (capillary filling, pressure driven-flow or electrically-driven transport) (Ezzatabadipour and Zahedi, 2021; Gerlero et al., 2021). It is therefore necessary to extend the existing models to a more general multiphysic approach that represents several transport phenomena at the same time, while avoiding the uncertain parameter τ in calculations.

Alternatively, one may introduce the well-known concept of periodically constricted tubes: a capillary bundle of parallel tubes, but now the pore radius is allowed to vary along the axial direction. Considering capillary tubes with periodic step changes of radius, from r_{max} to r_{min} and vice versa, yields $r_{eff} \sim (r_{min}^4)/(r_{max}^3)$ (Berli et al., 2017). For Whatman #1, assuming $r_{max} \sim 11\mu m$, one obtains $r_{min} \sim 3.1\mu m$. Although these values are physically sound, one is still dealing with a pair of unknown parameters (analogously to $r_{eff} = r_{pore}/\tau^2$), where at least one of them cannot be measured. The problem is inherited from the ambiguous inclusion of the hydrodynamic

and meniscus radius in the model, as mentioned above. In fact, the fluid dynamic problem itself suggests that there must be two relevant lengths characterizing the pore-scale geometry. In our present proposal, we stay in the scenario of the bundle of capillaries with periodically varying radii and include an innovative approach: the use of a probability density function to describe the pore radius distribution. Mathematically speaking, we are still dealing with the determination of two parameters (the mean and variance of the distribution), but these characteristic parameters are able to simultaneously represents four different transport phenomena (capillary filling, pressure-driven flow, electric transport, and electroosmotic flow), which constitutes a substantial gain in the route toward a generalized model of paper substrates.

The experimental validation was performed over two substrates frequently used in μPADs: Whatman #1 and Muntktell 00A filter papers. We report measurements of capillary imbibition, hydrostatic pressure-driven flow, and electrical resistance measurements. The proposed PDFs were evaluated by quantifying their predictions for the three experiments using a χ^2 test. The alternative modelling here presented enables a more general approach for describing the paper micro-structure with an arbitrary number of parameters. The model overcomes the previously reported single-physics approaches and can be also used as a valid strategy for the simultaneous estimation of several parameters that characterize the transport properties of paper, such as Darcy permeability, Washburn constant, or zeta potential, from simple and reproducible experimental results. Moreover, after defining a suitable PDF for each paper, the behavior of μPADs that combine different porous materials can be objectively evaluated.

2 Model formulation

Fig. 1 presents a simplified scheme of the proposed configuration for porous substrates as an arrangement of N_p parallel constricted tubes. In this case, the function $R(x)$ represents the constriction function, i.e. the tube radius as a function of distance x (the main direction for the fluid flow and electric field). Following this modelling strategy, the porosity can be calculated as:

$$\phi = \frac{N_p \int_0^L \pi R(x)^2 dx}{AL} \tag{1}$$

where A is the cross sectional area (commonly rectangular) and L is the length of the material considered.
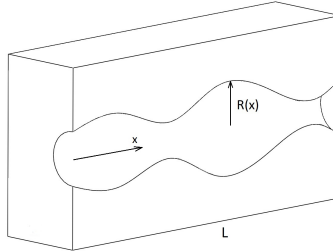

Fig. 1: Simplified scheme of the proposed configuration for a single constricted tube. The structure randomly repeats N_p times, without interconnections between neighbor tubes.

2.1 Hydrodynamic model

Considering that $R(x)$ is smooth along the $x-$axis and neglecting inertial effects (intra porous flow involves very low Reynolds numbers), one may use the Hagen-Poiseuille relation to calculate the flow rate through a single pore Q_h as follows (Reyssat et al., 2008):

$$Q_h = \frac{\Delta P \pi}{8\mu_\ell \int_0^L R(x)^{-4} dx} \tag{2}$$

where ΔP is the applied pressure difference and μ_ℓ is the liquid viscosity. Accounting for the N_p pores present in the substrate, the total flow rate is $Q_H = N_p Q_h$. Further, introducing Eq. 1 yields,

$$Q_H = \frac{\Delta P \phi A}{8\mu_\ell L} \frac{1}{\int_0^L R(x)^2 dx \int_0^L R(x)^{-4} dx}. \tag{3}$$

The $n-$th probability moment for the radius distribution is written as,

$$< R^n > \equiv \frac{\int_0^L R(x)^n dx}{L}.$$ (4)

Then, it is possible to define an equivalent hydraulic radius R_H as follows,

$$R_H \equiv \sqrt{\frac{Q_H 8 \mu_\ell L}{\Delta P \phi A}} = \sqrt{\frac{1}{< R^{-4} >< R^2 >}}$$ (5)

which represents the capillary radius of a bundle of uniform tubes exhibiting the overall flow rate Q_H. Equation 5 relates quantities that can be experimentally measured (first equality) to a certain combination of the probability moments of the radii distribution in the constricted tube model (second equality).

2.2 Capillary imbibition model

Capillary imbibition in porous materials has been extensively studied for more than 100 years and is currently an active topic of research (Cai et al., 2022; Piovesan et al., 2022). Capillary imbibition dynamics on a constricted tube (Fig 1) has been analyzed by different authors and can be modelled as (Young, 2004; Gorce et al., 2016; Reyssat et al., 2008):

$$\int_0^L R(l)^3 \left[\int_0^l \frac{dx}{R(x)^4} \right] dl = \frac{\gamma \cos \theta t_{fill}}{4 \mu_\ell}$$ (6)

where γ is the surface tension of liquid, θ is the contact angle of the advancing meniscus in the pores, and t_{fill} is the filling time. Given that porous morphology is uniform along the imbibition direction, i.e. the PDF is the same in all macroscopic regions, the definition of probability moment (Eq.4) can be also used in an intermediate length scale l (instead of L) to obtain:

$$\int_0^L R(l)^3 \left[\int_0^l \frac{dx}{R(x)^4} \right] dl = < R^{-4} > \int_0^L R(l)^3 l \, dl.$$

Moreover, a periodic radius profile can be used to estimate the last integral, taking $R(x) = R(x + n l_p)$, being n a natural number. If $L \gg l_p$ and $n l_p \approx L$,

$$\int_0^L R(l)^3 l \, dl \approx \int_0^{n l_p} R(l)^3 l \, dl = \sum_{i=1}^n \int_{(i-1)l_p}^{i l_p} R(l)^3 l \, dl$$

Considering that n is large, and the last integral is over one period, each term in the sum can be approximated by $< R^3 > i l_p^2$ and:

$$\int_0^L R(l)^3 l \, dl \approx < R^3 > l_p^2 \sum_{i=1}^n i \approx < R^3 > \frac{L^2}{2}$$

Using this approximation, Eq. 6 results:

$$< R^{-4} >< R^3 > \frac{L^2}{2} \approx \frac{\gamma \cos \theta t}{4 \mu_\ell}.$$ (7)

Finally, it is possible to define an equivalent capillary radius R_C of uniform tubes that produces the same infiltration rate:

$$R_C \equiv \frac{2 L^2 \mu_\ell}{\gamma \cos \theta t_{fill}} = \frac{1}{< R^{-4} >< R^3 >}.$$ (8)

This result is in accordance with previously reported calculations for sinusoidal constricted tubes and infiltration of mesoporous films (Sharma and Ross, 1991; Berli et al., 2017). In analogy to Eq. 5, Eq. 8 relates measurable quantities to a particular combination of the probability moments of the radii distribution in the constricted tube model. Moreover, after estimating R_C the Washburn coefficient D can be calculated as (Washburn, 1921):

$$D = \frac{\gamma \cos \theta R_C}{2 \mu_\ell}.$$ (9)

2.3 Electric Model

Keeping the hypothesis that $R(x)$ is smooth, the electric potential will be only function of x inside the tube. Also, if the electrical conductivity of fibers is negligible, the electrical resistance of a bundle of N_p parallel tubes can be calculated as:

$$R_p = \frac{\rho}{N_p} \int_0^L \frac{dx}{\pi R(x)^2}$$

where ρ represents the electrical resistivity. Introducing Eq. 1, the electrical resistance results:

$$R_p = \frac{\rho \int_0^L \pi R(x)^2 dx \int_0^L \frac{dx}{\pi R(x)^2}}{\phi A L}.$$

Using Eq. 4 leads to the following relationship between the paper electric resistance and the probability moments:

$$R_p \left(\frac{\phi A}{\rho L} \right) = < R^2 >< R^{-2} > . \tag{10}$$

The right hand side of Eq. (10) can be interpreted as a constriction factor (C) that always satisfies $C \geq 1$, being $C = 1$ in the case of uniform tubes. Then, the electrical resistance of saturated material is $\frac{\rho L}{\phi A}$, which represents an equivalent prism of resistivity ρ, section ϕA, and length L.

2.4 Electroosmotic flow model

Electroosmotic (EO) flow is generated when a potential difference $\Delta\Phi$ is applied to a saturated porous material that is electrically charged at the solid-liquid interface. The EO velocity can be calculated by the product of the EO permeability ($K_{eo} = \frac{\varepsilon\zeta}{\mu_\ell}$)[1] and the electric field ($E = \Delta\Phi/L$). Then, the EO flow rate for a single tube is (Probstein, 2005):

$$Q_{eo} = \bar{u}_{eo} \pi R^2 = \pi R^2 \frac{\varepsilon\zeta}{\mu_\ell} E$$

which can be rewritten as follows, after using Eq. 4,

$$Q_{eo} = \frac{\varepsilon\zeta}{\mu_\ell} \frac{\Delta\Phi}{\int_0^L \frac{dx}{\pi R(x)^2}}$$

Finally, considering N_p pores, the EO flow measured in the porous substrate is (Franck et al., 2021):

$$Q_{EO} = Q_{eo} N_p = \frac{\varepsilon\zeta}{\mu_\ell L} \frac{\Delta\Phi}{< R^{-2} >} \frac{\phi A L}{< R^2 >}$$

$$= \frac{\varepsilon\zeta\phi A}{\mu_\ell} \Delta\Phi \frac{1}{< R^{-2} >< R^2 >}$$

It is worth to mention here that one cannot determine the probability moments by a direct measurement of Q_{EO}, unless the ζ potential is known beforehand. However, since the expression for the probability moments agrees with the proposed for the electrical model, the term $\frac{1}{<R^{-2}><R^2>}$ can be obtained from electrical measurements and, consequently, the ζ potential could be determined from EO flow experiments (see section 4.3).

3 Experimental

3.1 Materials

Three types of experiments were conducted, wich are outlined in Fig. 2 and described in the following sections. Paper strips were cut from disks (Whatman #1, grade No. 1, 120 mm disc, Cityva, Marlborough, USA; Munktell, 00A, 125 mm disc, Munktell Filter AB, Falun, Sweden) following the machine direction (Elizalde et al., 2016). A solution of Tris-Acetate (12 mM Tris - 22 mM acetic acid, pH=4.78) was employed for electric experiments. Solution was characterized with a conductivity meter (Adwa AD 203, Szeged, Hungary) and electrical resistance was measured with a Picoammeter/Voltage Source (Keithley 6487, Cleveland, OH, USA). Devices were fabricated by laser-cutting (40 W CO$_2$ laser, Lasers Cuyana, San Rafael, Argentina) and hot lamination (DASA

---

[1] where ε is the electrical permittivity of the solvent and ζ the electrokinetic potential.

LM330) on both sides of the paper strips using 150 μm thick pouches (Binderplus, China) at 135 °C, at a constant speed of 3.5 mm/s. This setup minimizes the effects of evaporation on measurements. At both ends, symmetric 9 mm spaces were left for liquid reservoirs, by using a shorter lamination pouch on one side. A precision scale (Ohaus Pioneer, Parsippany, NJ, USA) was used for fluid dynamic and surface tension experiments. Acetic acid and tris were purchased from Laboratorios Cicarelli (Reagent SA, San Lorenzo, Argentina). All solutions were prepared with ultra pure water obtained from an inverse osmosis purifier (Osmoion, Apema SRL, Villa Dominico Argentina). The same water was used for hydrostatic pressure-driven and capillary-driven experiments. Highly hydrophobic double-sided adhesive tape (Stiko, Silkstone SA, Buenos Aires, Argentina) was used to fix the paper strips in all experiments. All measurements were made under controlled room conditions: 24 °C and 50 % relative humidity.
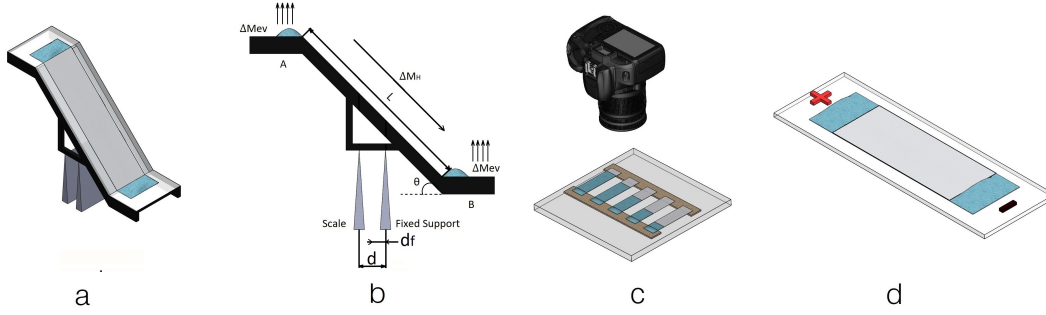

Fig. 2: Experimental setups of three different measurements: hydrostatic pressure-driven flow (a, b), capillary-driven flow (c), and electric current through the saturated paper (d).

3.2 Hydrostatic pressure-driven flow experiments

In this section the experiments associated with Eq. 5 are presented. The experimental setup employed is shown in Fig. 2a and 2b, which is similar to the one used in a previous work (Franck et al., 2021). A scale and a system of blades were used to amplify the measured weight of liquid in the reservoirs. The liquid was driven by the action of gravity through the inclined ramp draining the upper reservoir and filling the lower one. One blade was attached to a fixed support and the other one was placed over the scale. In this configuration, the scale records the change of mass distribution produced by the liquid flow in the paper strip. This scheme amplifies the force over the scale and balances the effects of evaporation, as it will be discussed below. The paper strip of length L, width W, thickness h was tilted at the angle θ (Fig. 2a). The blades were separated by a distance d, and the center of mass was located at a distance d_f from the fixed blade (Fig 2b). The mass variation actually recorded by the scale was determined by the flow of liquid between the reservoirs (ΔM_H) and the change in mass due to evaporation (ΔM_{ev}) that occurs at each reservoir, which was assumed to be identical on both sides. It is important to note that these phenomena were not equally amplified by the experimental scheme. While the flow between the reservoirs was amplified as,

$$\Delta M^H = \Delta M_H \frac{L\cos\theta}{d}, \tag{11}$$

where superscripts and subscripts denote mass change with and without amplification, respectively, the mass change due to evaporation was amplified as,

$$\Delta M^{ev} = \Delta M_{ev} \frac{d_f}{d}. \tag{12}$$

Then, the change in mass effectively recorded by the scale ΔM^s is given by:

$$\Delta M^s = \Delta M^H + \Delta M^{ev}.$$

It is worth to note that the amplification factor in ΔM^{ev} can be minimized by selecting a small value of d_f (placing the reservoirs symmetrically to the fixed support). Moreover, the amplification factors in Eqs.11 and 12 can be experimentally evaluated by a calibration procedure (Franck et al., 2021). A known mass of liquid ΔM_0 was added to the reservoir 1 (Fig. 2b) and the mass increase in the scale ΔM^A was registered. Alternatively, the same

mass was added to the reservoir 2 and the mass variation ΔM^B was registered. Then, the amplification factors were calculated as:

$$\frac{L\cos\theta}{d} = \frac{\Delta M^A - \Delta M^B}{\Delta M_0} \tag{13}$$

and

$$\frac{d_f}{d} = \frac{(\Delta M^B - \Delta M^A)}{2\Delta M_0} \frac{\frac{\Delta M^A}{\Delta M^B} + 1}{-\frac{\Delta M^A}{\Delta M^B} + 1} \tag{14}$$

Details about of the derivation of these expressions can be found in the Supplementary Information. For the experiments presented in this work, typical amplification factors were $\frac{L\cos\theta}{d} \approx 25$ and $\frac{d_f}{d} \approx 0.5$. In order to determine ΔM_{ev}, the complete system was supported by the scale by setting the two blades over the scale plate, thus the registered mass change was $2\Delta M_{ev}$. Consequently, the volumetric flow rate Q_H can be calculated by

$$Q_H = \frac{\Delta M_H}{\rho \, \Delta t} \tag{15}$$

and the pressure difference ΔP can be related to the height difference by:

$$\Delta P = \rho g L \sin\theta. \tag{16}$$

Finally, the values calculated through Eq. 15 and 16 can be replaced in Eq. 5 to obtain the R_H.

3.3 Capillary imbibition experiments

In this section the experiments associated with Eq. 8 are presented. The employed experimental setup (Fig. 2c) is similar to the one used by Elizalde et al. (2016). In these experiments, the wetting front position is recorded over time, which enables the calculation of the effective capillary radius R_C (Eq. 8). To determine R_C, the contact angle was considered as $\theta = 0$ (Elizalde et al., 2016) and the effective surface tension of the deionized water in paper, $\gamma = 40 \times 10^{-3}\,\text{N/m}$. This value of surface tension is smaller than the obtained for pure water ($\sim 74 \times 10^{-3}\,\text{N/m}$), probably due to the dissolution of some components present in the paper fibers (Elizalde et al., 2016). The effective surface tension was obtained through additional experiments, which are reported in the Supplementary Information.

Ten rectangular paper strips for each type of paper were laser cut 10 mm width and 30 mm length and were mounted over a glass support. Hydrophobic double-sided adhesive tape was placed at the ends to fix the strips and to delimit the water reservoir. The strips were arranged keeping an air gap between the glass avoiding edge effects that could alter the imbibition flow (Schaumburg and Berli, 2019). Experiments were recorded by using a high resolution digital camera (Canon EOS 1000D). The microfluidic strips were placed horizontally and back-lit with a white LED lamp where irradiation was kept on a low value to avoid temperature increase. The camera was placed vertically at a distance of 30 cm, connected to a PC, and set to burst mode. The spatial resolution was 36 μm and the time resolution was 12 frames per minute. Experimental runs start when a small volume of deionized water was poured into the inlet reservoir. Image prostprocessing to extract the fluid front position as a function of time was implemented as follows: (i) the area of interest was taken as the central 90% of each paper strip width to avoid edge effects; (ii) paper strip area was processed to obtain a normalized grey scale matrix. The procedure involves subtraction of the first image to each image and then normalization by the last one. The resulting matrix was laterally averaged, thus obtaining a longitudinal saturation profile; (iii) the front position in each profile was determined at 25 % of saturated luminosity value.

3.4 Electrical resistance experiments

In this section the experiments associated with Eq. 10 are presented. Electrically-driven measurements were carried out to determine the resistance of the saturated paper (Fig. 2d). Different electrolyte solutions were used to measure different free solution conductivities, in order to improve the estimation of the left hand side (LHS) of Eq. 10. Platinum electrodes were connected to the liquid reservoirs, and a constant difference potential was applied through the paper strips, which were 10 mm width and 40 mm length. Low voltages ($\approx 10\,\text{V}$) were used to minimize the effects of both Joule heating and EO flow. Free solution liquid resistivities (ρ) were measured with a conductivity meter. To extend the range of solution concentration that can be used in the experiments, electric resistance was measured in a calibrated capillary by applýing 10 V difference potential using platinum electrodes.

4 Results and discussion

4.1 Experimental results

Hydrodynamic experiments were performed as discussed in section 3.2 to assess the LHS of Eq.5. Figure 3 present the results of these measurements. The first part of the plot, colored in blue, corresponds to the calibration of the system. After completely filling the paper strip with water (not shown in the figure), two 50 μL drops were consecutively placed in the upper reservoir. The scale measured a mass increase ΔM^{A1} and ΔM^{A2} respectively. The opposite occured when the drops were placed in the lower reservoir: a reduction of the mass was recorded. The amplification factors can be determined by averaging the measured values of ΔM^A, ΔM^B and using Eqs. 13 and 14. Afterwards, the liquid steadily flowed from the highest to the lowest reservoir, while data were recorded over time (black dots), after a small initial step allowed for system stabilization. The curve slope was determined with a linear fit (red line) and then used to obtain R_H in Eq. 5.
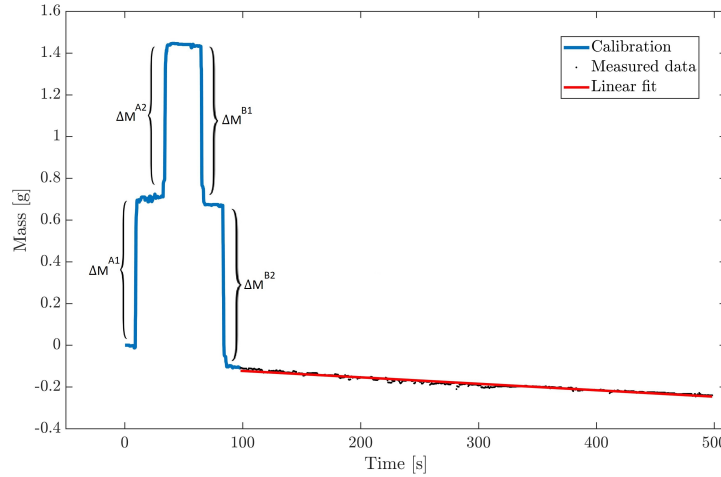

Fig. 3: Calibration process (blue line), determining ΔM^A and ΔM^B variations when known volume droplets are placed in reservoirs *A* and *B* respectively. This procedure can be used to obtain amplification factors of the system. Stabilized region (black dots) can be used to measure the flow rate through the paper strip.

The measured ΔM^s value in this case was $\approx 3.4 \times 10^{-4}$ g/sec. The mass flow and evaporation amplification factors were 29 and -0.69, respectively. The negative sign of d_f means that the reservoirs center of mass is at the right of the fixed blade (Fig. 2b). Certainly, the center of mass of the whole system is however between the blades to ensure mechanical stability. Furthermore, the ΔM_{ev} measured in this case was 3.33×10^{-5} g/sec. It is important to note that this value is comparable to, even larger than, the hydrodynamic flow rate through the paper strip ($\Delta M_H = 1.25 \times 10^{-5}$ g/sec) obtained from Eq. 11. The proposed experimental setup allows one to clearly distinguish between both magnitudes given the high ratio between the respective amplification factors.Capillary filling experiments were performed as discussed in section 3.3 to asses the LHS of Eq. 8. Figure 4 shows several experiments of the fluid front imbibition dynamics for different substrates (Whatman # 1 and Munktell 00A). The squared position as a function of time shows a linear correlation ($L^2 = Dt$), as it is expected for systems satisfying the the Lucas-Washburn law (Lucas (1918), Washburn (1921)). In fact, the slope in this figure can be associated with a diffusive coefficient D (known as Washburn coefficient) that depends on the paper substrate and physical properties of the liquid (Eq. 8). The measured values are summarized in Table 1. Two groups of lines can be identified in Figure 4, which correspond to the different paper substrates. The dispersion of D values for each paper corresponds to that found in previous works (Elizalde et al., 2016), which is around 7%. The average of D values, however, are smaller than those found on such previous work, due to the use of laminated paper strips on both sides, which modifies the imbibition dynamics.
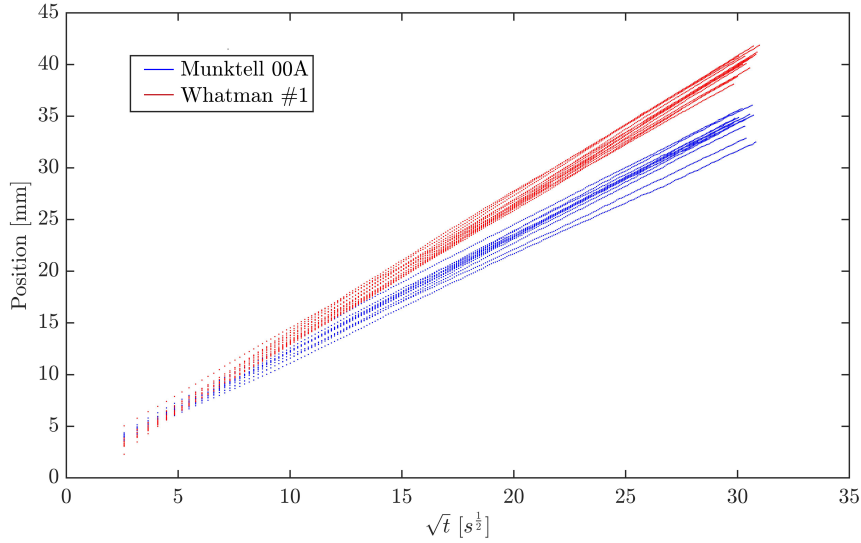
Fig. 4: Fluid front position as a function of square root of time, for the capillary filling of Whatman #1 and Munktell 00A papers along the machine direction. Different slopes indicate typical variations of R_C and D values obtained in identical paper strips (Eqs. (8) and (9), respectively).

The last set of experiments corresponds to the electrical conductivity measurements made for both capillary tube (free solution) and paper substrates. The results obtained via direct measurements with the conductimeter and through the capillary matched those theoretically predicted for the electrolyte concentration at room temperature. Figure 5 shows the results for several electrolyte solutions with different conductivities. The linearity of the plot indicates good data correlation, as well as negligible interference from Joule heating effects or EO flow.
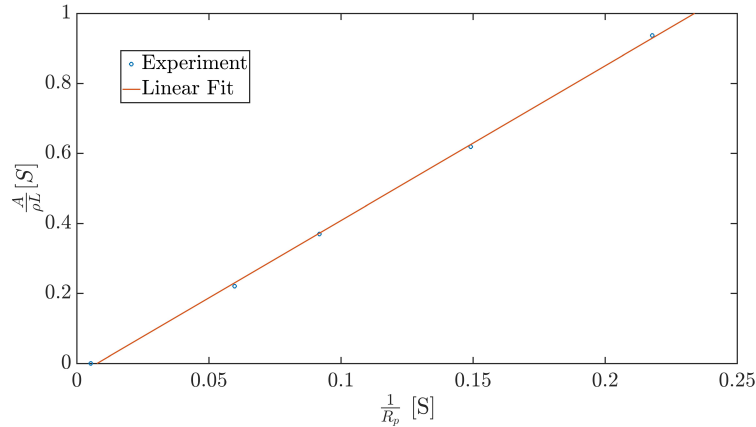

Fig. 5: Calculated free flow conductance as a function of the electric conductance in Whatman #1 substrate. Constriction factor (C) can be obtained from the slope of the linear fit, according to Eq. (10).

4.2 Pore size distribution

Three different PDFs were tested in order to optimize the description of pore size distribution: (i) bimodal distribution consisting in two delta Dirac's functions that represent the radii with an equal probability of occurrence ; (ii) arcsine distribution, which models radii as an oscillating sine wave between R_{max} and R_{min}); and (iii) log-normal continuous probability distribution. Fig. 6 a and b show an schematic representation of these distributions. These distributions can be completely characterized by two free parameters, and they were have been previously used to describe similar systems (Sharma and Ross, 1991; Berli et al., 2017; Lei et al., 2021; Apostolopoulou et al., 2020; Aramideh et al., 2018). Bimodal and arcsine distributions have the advantage of being physically and mathematically simple; both density functions can be analytically handled. However, the range of pore sizes they can explore are bounded (discrete in the case of the bimodal), which limits the description of the pore morphology arising in paper substrates. On the other hand, the log-normal distribution is more complex to handle, but it

entails the possibility of wide and continuum variations of pore sizes (Fig. 6a), which allows one to reproduce the geometry of the substrate with greater precision. The log-normal distribution will be further described next; while the description both bimodal and arcsine distributions are reported in the Supplementary Information.
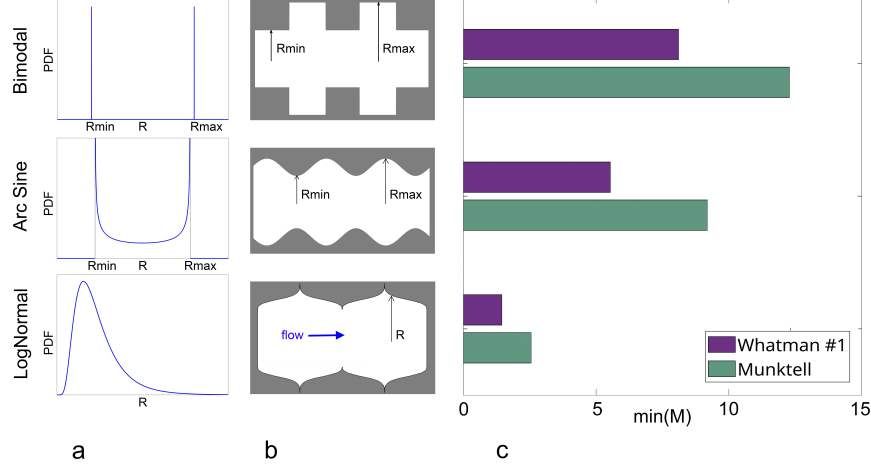

Fig. 6: PDFs explored in modeling: (a) plots of probability densities as a function of radius, (b) schematic representations of pore shapes and characteristic radii, (c) performance of each PDF to describe experimental data from two different substrates, as characterized by the χ^2 test.

The log-normal PDF is defined as:

$$f(R) = \frac{1}{R\sigma\sqrt{2\pi}} e^{-\frac{(\ln R - \mu)^2}{2\sigma^2}} \tag{17}$$

where the random variable R represents a specific radius. The parameters μ and σ define the arithmetic mean ($E[R]$) and variance ($Var[R]$) as follows:

$$E[R] = e^{\mu + \frac{\sigma^2}{2}} = X \tag{18}$$

$$Var[R] = e^{2\mu + \sigma^2}(e^{\sigma^2} - 1) \tag{19}$$

To evaluate the performance of the model with this radius distribution, a figure of merit M was constructed using the predicted results for the three performed experiments. The measured values of R_H, R_C and C were compared against the model predicted values $R_H(\mu, \sigma)$, $R_C(\mu, \sigma)$ and $C(\mu, \sigma)$, respectively, for different combinations of μ and σ. Each predicted value can be calculated using the PDF to evaluate the probability moments (Eq. (4)) in Eqs. (5), (8) and (10), respectively. The differences were weighed by the experimental dispersion of each magnitude to obtain a Chi-square type distribution (Press et al., 1986). The final expression of the figure of merit was,

$$M(\mu, \sigma) = \frac{(R_H - R_H(\mu, \sigma))^2}{Var[R_H]} + \frac{(R_C - R_C(\mu, \sigma))^2}{Var[R_C]} + \frac{(C - C(\mu, \sigma))^2}{Var[C]}$$

Since there are three measured values and two free parameters, this distribution has a degree of freedom of one, in which the 95% confidence level region is achieved for values of $M < 3.84$ (Abramowitz and Stegun, 1965).
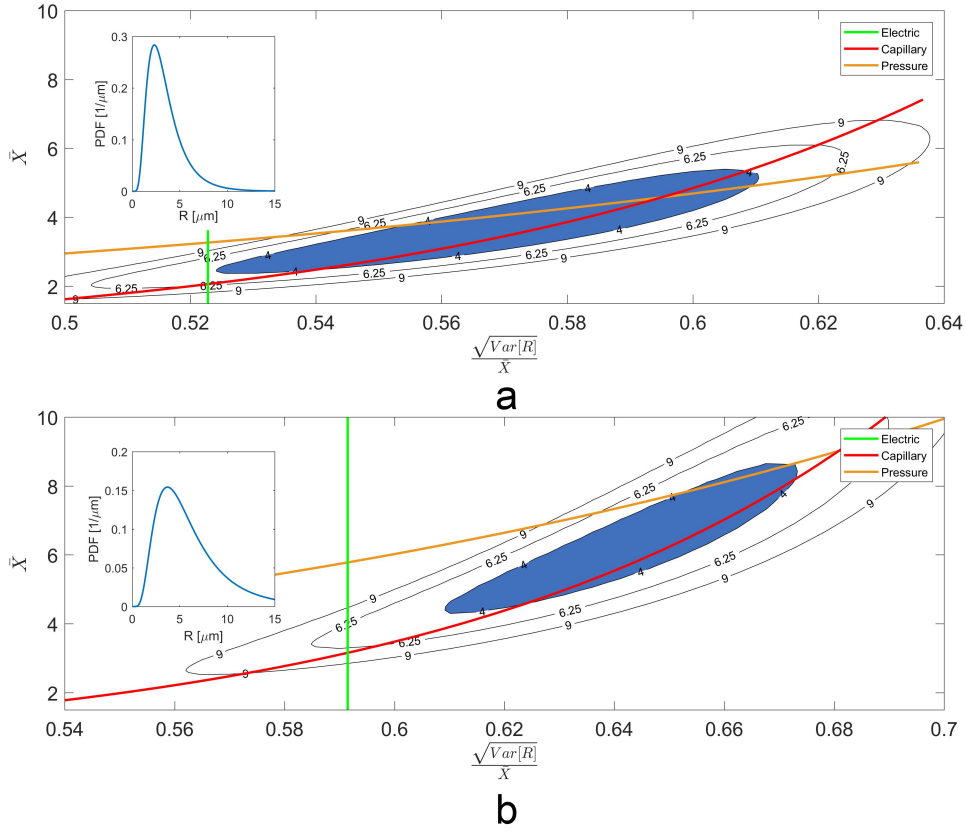
Fig. 7: Contour map values of M using the log-normal distribution for Whatman #1 (a) and Munktell 00A (b). Solid lines indicate the values for which the parameter combination of PDF reproduces the experimental results of R_H (orange line), R_C (red line), and C (green line). The colored (blue) region corresponds to $M < 3.84$, which represents the 95% confidence region for the predicted parameters. The insets on the left show the optimal log-normal PDF that produce the minimum value of M.

Figure 7 shows contour maps of M obtained by using the log-normal distribution, for the two paper substrates. The results are presented in the transformed variables X and $\sqrt{Var[R]}/X$ for a better visualization. This configuration also enables a direct comparison to other probability distributions (see the Supplementary Information for details). The minimum M values obtained for different PDFs are shown in Fig. 6d for the two paper substrates. From these results, it is clear that the log-normal distribution has a better performance to simultaneously represent the response of the three experiments. The optimum parameter combination (minumum M) can be used to obtain the model prediction for each experiment. The overall results are summarized in Table 1. Also in Figure 7, the combinations of μ and σ that satisfy $R_H - R_H(\mu, \sigma) = 0$ (orange line), $R_C - R_C(\mu, \sigma) = 0$ (red line), and $C - C(\mu, \sigma) = 0$ (green line) are shown. These lines indicate the regions where the model independently reproduces each experimental result. The blue colored zones are limited by $M < 3.84$ and indicate the 95% confidence regions for the predicted parameters. Ideally, all the three lines should cross in a single point, which means that for different experiments the model predicts the same radius distribution, with an unique combination of mean radius and variance. The distance between the crossing points is an indicator of the model accuracy for the chosen PDF. Particularly, electrical measurements (vertical green lines) indicate that the factor C is independent of the mean value of the distribution X. In fact, a multiplicative factor in the distribution radius does not change neither C nor the $\sqrt{Var[R]}/X$ parameter. On the other hand, results from capillary-driven flow (red line) and hydrostatic pressure-driven flow (orange line) depend on both variables. Regarding paper substrates, one observes that data cloud for Munktell has a larger error than for Whatman #1, which means that the model capture the experiments with lower fidelity for Munktell than for Whatman #1. In fact, the minimum of the function M determine the PDF parameters that better describe the experimental data. In the case of the Whatman #1 paper, the minimum corresponds to $\mu = 1.12$ and $\sigma = 0.52$, which in turn correspond to $X = 3.5\,\mu m$ and $\sqrt{Var[R]} = 6.1\,\mu m$ (see the inset in Fig. 7a). In the case of Munktell paper, the optimum values are $\mu = 1.65$ and $\sigma = 0.586$, which correspond to $X = 3.5\,\mu m$ and $\sqrt{Var[R]} = 15.5\,\mu m$ (see the inset in Fig. 7b).

4.3 Comparison between different models

In order to emphasize the advantages the multiphysic model, we present the direct link between the PDFs and some well-known parameters from single-physics models, such as Darcy's permeability K, Washburn coefficient D, and electrokinetic potential ζ. Additionally, the constriction factor (C), the equivalent radii for hydrodynamic (R_H) and capillary phenomena (R_C) are reported for both substrates. To summarize this information, two types of data are presented in Table 1: (i) from measurements, with values and uncertainties related to each set of experiments (*Measurement*) and (ii) from model, using the best fitted values according to minimum M (*Model prediction*).

Table 1: Parameters for single-physics models related to different radii statics in the present work. Electroosmotic permeability (K_{eo}) was obtained from Franck et al. (2021) for pH=4.7 solution at $E = 2.5\,\mathrm{kV/m}$.

Substrate		**Whatman #1**		**Munktell 00A**	
Magnitude	Definition	Measurement	Model prediction	Measurement	Model prediction
Equivalent hydrodynamic radius [μm]	$R_H=\sqrt{\frac{1}{<R^{-4}><R^2>}}$	0.86 ± 0.08	0.79	1.1 ± 0.1	0.93
Darcy permeability $\times10^{-14}$[m^2]	$K=\frac{R_H^2}{8}$	9.3 ± 0.9	7.8	13 ± 1	10.9
Equivalent capillary radius [μm]	$R_C=\frac{1}{<R^{-4}><R^3>}$	0.089 ± 0.008	0.096	0.064 ± 0.006	0.07
Washburn coefficient $\times10^{-6}$ [$\frac{\mathrm{m}^2}{\mathrm{s}}$]	$D=\frac{\gamma\cos\theta R_C}{2\mu_\ell}$	1.8 ± 0.2	1.9	1.3 ± 0.1	1.4
Constriction factor	$C=<R^2><R^{-2}>$	2.6 ± 0.3	3.1	3.3 ± 0.3	4
Zeta potential [mV]	$\zeta_p=\frac{K_{eo}\mu_\ell C}{\varepsilon\phi}$	2.8 ± 0.3	3.3	5.3 ± 0.5	6.4

The results in Table 1 show that the deviations between the measurement and the model predictions are relatively small, most of them within the range of the measurement uncertainty. It is worth to mention here that the model captures the fact that R_H is about ten times larger than R_C in paper substrates. This apparent discrepancy, which is known in the microfluidics community (Alava et al., 2004), is inherent to the extrapolation of capillary-driven flow models from single tubes to porous media: the main pitfall is considering a unique pore radius for both Laplace pressure and fluid resistance. Regarding EO flow, one may note that the value obtained for the constriction factor is comparable to the value of tortuosity calculated for electrokinetic and EO phenomena by Gerlero et al. (2021), while being different to those predicted for fluid transport (Matyka et al., 2008). Finally, it is necessary to remark that these reported values correspond to both sides laminated paper, and could differ from other results where paper was not laminated or single side-laminated (Noh and Phillips, 2010; Elizalde et al., 2016).

5 Conclusions

This paper proposes an innovative approach that considers the pore space as a bundle of periodically constricted tubes modelled through a PDF of the porous radii, which can simultaneously represent four different transport phenomena in porous substrates: capillary filling, pressure-driven flow, electric transport, and electroosmotic flow. The mathematical basis of the model were described and the model predictions were experimentally validated by using well-known filter papers. The proposed model enabled the characterization of porous substrates by means of a reduced number of parameters (two free parameters describing the radius distribution). In relation to single-physics models, the multiphysics approach avoids the concept of tortuosity (τ), which is normally used as an adjustment variable. Although τ is a widely used parameter, its value strongly depends on the experiment under consideration and can be much larger than expected for the paper morphology. In contrast, the constricted tube model can reasonably reproduce the results obtained in all the experiments studied using a single PDF.

Typical parameters values for Whatman #1 and Munktell 00A papers are provided for double laminated substrates aimed to improve the prediction capability of most of μ-PADs developers working with such materials. The fact that fluid and charge transport phenomena are satisfactorily described by a single topological scheme confirms that the proposed model entails a more generalized view of the underlying physics.

This model's feature definitely improves the prediction capabilities because, performing only two of the proposed experiments, a given substrate can be fully characterized for any of the studied processes (capillary filling, pressure driven flow, electroosmotic flow, and electric current driving). Furthermore, after having characterized different substrates, developers can use different combination of papers for creating arbitrary multi-substrates arrangements. The behavior of these complex heterogeneous μPADs can be predicted through an equivalent PDF made as the weighted sum of single paper PDFs. Finally, it is important to note that the proposed model can be applied to porous media different from paper by simply selecting the suitable pore distribution function.

Conflict of interest

The authors declare that they have no conflict of interest.

Data avilability statement

The datasets generated during and analysing the current study are available from the corresponding author on reasonable request.

Supplementary information

Supplementary information providing experimental data on surface tension measurements, as well as the results of χ^2 test of other PDFs, can be found in the on-line version of the article.

References

Abramowitz M, Stegun IA (1965) Handbook of Mathematical Functions. American Association of Physics Teachers

Alava M, Dubé M, Rost M (2004) Imbibition in disordered media. Adv Phys 53(2):83–175

Apostolopoulou M, Stamatakis M, Striolo A, Dusterhoft R, Hull R, Day R (2020) A novel modeling approach to stochastically evaluate the impact of pore network geometry, chemistry and topology on fluid transport. Transport Porous Med 136(2):495–520

Aramideh S, Vlachos PP, Ardekani AM (2018) Pore-scale statistics of flow and transport through porous media. Phys Rev E 98:013104

Archie G (1942) The Electrical Resistivity Log as an Aid in Determining Some Reservoir Characteristics. T Soc Petrol En AIME 146(01):54–62

Bear J (1972) Dynamics of Fluids in Porous Media. American Elsevier Publishing Company, New York, USA.

Bear J, Cheng AHD (2010) Modeling groundwater flow and contaminant transport, vol 23. Springer Science & Business Media, Dordrecht, Netherlands

Berg C (2014) Permeability description by characteristic length, tortuosity, constriction and porosity. Transport in Porous Media 103:381–400

Berli CL, Mercuri M, Bellino MG (2017) Modeling the abnormally slow infiltration rate in mesoporous films. Phys Chem Chem Phys 19(3):1731–1734

Bussian AE (1983) Electrical conductance in a porous medium. Geophysics 48(9):1258–1268

Böhm A, Carstens F, Trieb C, Schabel S, Biesalski M (2014) Engineering microfluidic papers: Effect of fiber source and paper sheet properties on capillary-driven fluid flow. Microfluid Nanofluid 16:789–799

Cai J, Perfect E, Cheng CL, Hu X (2014) Generalized modeling of spontaneous imbibition based on hagen–poiseuille flow in tortuous capillaries with variably shaped apertures. Langmuir 30(18):5142–5151

Cai J, Chen Y, Liu Y, Li S, Sun C (2022) Capillary imbibition and flow of wetting liquid in irregular capillaries: A 100-year review. Advances in Colloid and Interface Science 304:102654

Cummins BM, Chinthapatla R, Ligler FS, Walker GM (2017) Time-dependent model for fluid flow in porous materials with multiple pore sizes. Anal Chem 89(8):4377–4381

Duda A, Koza Z, Matyka M (2011) Hydraulic tortuosity in arbitrary porous media flow. Phys Rev E Stat Nonlin Soft Matter Phys 84(3 Pt 2):036319

Elizalde E, Urteaga R, Berli CLA (2016) Precise capillary flow for paper-based viscometry. Microfluid Nanofluid 20(10):1–8

Ezzatabadipour M, Zahedi H (2021) A novel method for streamline-based tortuosity calculation and investigation of obstacles shape effect on tortuosity in porous media with random elliptical obstacles using lattice boltzmann method. Transport Porous Med 136(1):103–124

Franck N, Schaumburg F, Kler PA, Urteaga R (2021) Precise electroosmotic flow measurements on paper substrates. Electrophoresis 42(7-8):975–982

Gerlero GS, Damián SM, Schaumburg F, Franck N, Kler PA (2021) Numerical simulations of paper-based electrophoretic separations with open-source tools. Electrophoresis 42:1543–1551

Gerlero GS, Valdez AR, Urteaga R, Kler PA (2022) Validity of capillary imbibition models in paper-based microfluidic applications. Transport Porous Med pp 1–20

Ghanbarian B, Hunt AG, Ewing RP, Skinner TE (2014) Universal scaling of the formation factor in porous media derived by combining percolation and effective medium theories. Geophys Res Lett 41(11):3884–3890

Gorce JB, Hewitt IJ, Vella D (2016) Capillary imbibition into converging tubes: beating washburn's law and the optimal imbibition of liquids. Langmuir 32(6):1560–1567

Gruener S, Sadjadi Z, Hermes HE, Kityk AV, Knorr K, Egelhaaf SU, Rieger H, Huber P (2012) Anomalous front broadening during spontaneous imbibition in a matrix with elongated pores. P Natl Acad Sci USA 109(26):10245–10250

Herrick DC, Kennedy WD (1994) Electrical efficiency—a pore geometric theory for interpreting the electrical properties of reservoir rocks. Geophysics 59(6):918–927

Kozeny M (1927) Uber kapillare leitung des wassers im boden. Sitzber Akad Wiss Wein, Math-naturw 136:Abt. II a, P. 277

Lei J, Xu Z, Xin F, Lu TJ (2021) Dynamics of capillary flow in an undulated tube. Phys Fluids 33(5):052109

Liu Z, He X, Han J, Zhang X, Li F, Li A, Qu Z, Xu F (2018) Liquid wicking behavior in paper-like materials: mathematical models and their emerging biomedical applications. Microfluid Nanofluid 22(11):1–20

Lucas R (1918) Ueber das Zeitgesetz des kapillaren Aufstiegs von Flüssigkeiten. Colloid & Polymer Science 23(1):15–22

MacDonald BD (2018) Flow of liquids through paper. J Fluid Mech 852:1–4

Mai VP, Ku CH, Yang RJ (2019) Porosity estimation using electric current measurements for paper-based microfluidics. Microfluid Nanofluid 23(4):1–10

Masoodi R, Pillai KM (2010) Darcy's law-based model for wicking in paper-like swelling porous media. AIChE J 56(9):2257–2267

Matyka M, Khalili A, Koza Z (2008) Tortuosity-porosity relation in porous media flow. Phys Rev E 78(2):026306

Modha S, Castro C, Tsutsui H (2021) Recent developments in flow modeling and fluid control for paper-based microfluidic biosensors. Biosens Bioelectron p 113026

Mora MF, Garcia CD, Schaumburg F, Kler PA, Berli CL, Hashimoto M, Carrilho E (2019) Patterning and modeling three-dimensional microfluidic devices fabricated on a single sheet of paper. Anal Chem 91(13):8298–8303

Noh H, Phillips ST (2010) Metering the capillary-driven flow of fluids in paper-based microfluidic devices. Anal Chem 82(10):4181–4187

Piovesan A, Nicasy R, Arens T, Dequeker B, Soete J, Achille C, Dochy R, Parra-Cabrera C, Ameloot R, Verboven P, Nicolai B (2022) Multiscale modelling of capillary imbibition in 3d-printed porous microfluidic channels. Microfluid Nanofluid 26(3):1–15

Press WH, Vetterling WT, Teukolsky SA, Flannery BP (1986) Numerical recipes, vol 818. Cambridge university press, Cambridge, UK.

Probstein RF (2005) Physicochemical hydrodynamics: an introduction. John Wiley & Sons, Newark, NJ, USA.

Reyssat M, Courbin L, Reyssat E, Stone HA (2008) Imbibition in geometries with axial variations. J Fluid Mech 615:335–344

Salama A, Cai J, Kou J, Sun S, El-Amin MF, Wang Y (2021) Investigation of the dynamics of immiscible displacement of a ganglion in capillaries

Schaumburg F, Berli CL (2019) Assessing the rapid flow in multilayer paper-based microfluidic devices. Microfluid Nanofluid 23(8):1–10

Schaumburg F, Kler PA, Berli CLA (2018a) Numerical prototyping of lateral flow biosensors. Sensor Actuat B-Chem 259:1099–1107

Schaumburg F, Urteaga R, Kler PA, Berli CL (2018b) Design keys for paper-based concentration gradient generators. J chromatogr A 1561:83–91

Schaumburg F, Kler PA, Berli CL (2020) Comprehensive model of electromigrative transport in microfluidic paper based analytical devices. Electrophoresis 41(7-8):598–606

Scheidegger AE (1974) The Physics of Flow Through Porous Media (3rd Edition). University of Toronto Press, Toronto, Canada.

Sharma R, Ross DS (1991) Kinetics of liquid penetration into periodically constricted capillaries. J Chem Soc Faraday T 87(4):619–624

Shen F, Ai M, Li Z, Lu X, Pang Y, Liu Z (2021) Pressure measurement methods in microchannels: advances and applications. Microfluid and Nanofluid 25(5):1–31

Tesfaye T, Hussen A (2022) Microfluidic paper-based analytical device (μpad) fabricated by wax screen printing technique for the determination of nitrite and nitrate ion in water samples. Microfluid Nanofluid 26(3):1–13

Urteaga R, Elizalde E, Berli CL (2018) Transverse solute dispersion in microfluidic paper-based analytical devices (μpads). Analyst 143(10):2259–2266

Washburn EW (1921) The dynamics of capillary flow. Phys Rev 17(3):273

Young WB (2004) Analysis of capillary flows in non-uniform cross-sectional capillaries. Colloid Surface A 234(1-3):123–128